Biomedical Optics EXPRESS

Spectral domain detection in low-coherence spectroscopy

Nienke Bosschaart,[1,*] Maurice C. G. Aalders,[1] Ton G. van Leeuwen,[1,2] and Dirk J. Faber[1]

[1]*Biomedical Engineering and Physics, Academic Medical Center, University of Amsterdam, P.O. Box 22700, NL-1100 DE Amsterdam, The Netherlands*
[2]*Biomedical Photonic Imaging Group, University of Twente, P.O. Box 217, NL-7500 AE Enschede, The Netherlands*
**n.bosschaart@amc.uva.nl*

Abstract: Low-coherence spectroscopy (LCS) offers the valuable possibility to measure quantitative and wavelength resolved optical property spectra within a tissue volume of choice that is controllable both in size and in depth. Until now, only time domain detection was investigated for LCS (tdLCS), but spectral domain detection offers a theoretical speed/sensitivity advantage over tdLCS. In this article, we introduce a method for spectral domain detection in LCS (sdLCS), with optimal sensitivity as a function of measurement depth. We validate our method computationally in a simulation and experimentally on a phantom with known optical properties. The attenuation, absorption and scattering coefficient spectra from the phantom that were measured by sdLCS agree well with the expected optical properties and the measured optical properties by tdLCS.

OCIS codes: (030.1640) Coherence; (300.6190) Spectrometers; (160.4760) Optical properties; (170.6510) Spectroscopy, tissue diagnostics.

References and links

1. N. Bosschaart, M. C. G. Aalders, D. J. Faber, J. J. A. Weda, M. J. C. van Gemert, and T. G. van Leeuwen, "Quantitative measurements of absorption spectra in scattering media by low-coherence spectroscopy," Opt. Lett. **34**(23), 3746–3748 (2009).
2. N. Bosschaart, D. J. Faber, T. G. van Leeuwen, and M. C. G. Aalders, "Measurements of wavelength dependent scattering and backscattering coefficients by low-coherence spectroscopy," J. Biomed. Opt. **16**(3), 030503 (2011).
3. N. Bosschaart, D. J. Faber, T. G. van Leeuwen, and M. C. G. Aalders, "*In vivo* low-coherence spectroscopic measurements of local hemoglobin absorption spectra in human skin," J. Biomed. Opt. **16**(10), 100504 (2011).
4. R. Leitgeb, C. K. Hitzenberger, and A. F. Fercher, "Performance of fourier domain vs. time domain optical coherence tomography," Opt. Express **11**(8), 889–894 (2003).
5. D. J. Faber and T. G. van Leeuwen, "Optical coherence tomography," in *Optical-Thermal Response of Laser-Irradiated Tissue*, A. J. Welch and M. J. C. van Gemert, eds. (Springer Science & Business Media, 2010), Chap. 18.
6. R. Leitgeb, M. Wojtkowski, A. Kowalczyk, C. K. Hitzenberger, M. Sticker, and A. F. Fercher, "Spectral measurement of absorption by spectroscopic frequency-domain optical coherence tomography," Opt. Lett. **25**(11), 820–822 (2000).
7. A. Wax, C. Yang, and J. A. Izatt, "Fourier-domain low-coherence interferometry for light-scattering spectroscopy," Opt. Lett. **28**(14), 1230–1232 (2003).
8. F. Robles, R. N. Graf, and A. Wax, "Dual window method for processing spectroscopic optical coherence tomography signals with simultaneously high spectral and temporal resolution," Opt. Express **17**(8), 6799–6812 (2009).
9. D. J. Faber and T. G. van Leeuwen, "Doppler calibration method for spectral domain OCT spectrometers," J Biophotonics **2**(6-7), 407–415 (2009).
10. J. Zhang, J. S. Nelson, and Z. Chen, "Removal of a mirror image and enhancement of the signal-to-noise ratio in Fourier-domain optical coherence tomography using an electro-optic phase modulator," Opt. Lett. **30**(2), 147–149 (2005).
11. N. Nassif, B. Cense, B. Park, M. Pierce, S. Yun, B. Bouma, G. Tearney, T. Chen, and J. de Boer, "*In vivo* high-resolution video-rate spectral-domain optical coherence tomography of the human retina and optic nerve," Opt. Express **12**(3), 367–376 (2004).
12. G. Häusler and M. Linder, "Coherence radar and spectral radar—new tools for dermatological diagnosis," J. Biomed. Opt. **3**(1), 21–31 (1998).

#171508 - $15.00 USD Received 27 Jun 2012; revised 6 Aug 2012; accepted 13 Aug 2012; published 27 Aug 2012

13. Data tabulated from various sources compiled by S. Prahl, "Optical properties spectra," *http://omlc.ogi.edu/spectra*.
14. F. E. Robles, C. Wilson, G. Grant, and A. Wax, "Molecular imaging true-colour spectroscopic optical coherence tomography," Nat. Photonics **5**(12), 744–747 (2011).

1. Introduction

Low-coherence spectroscopy (LCS) is a method for simultaneous measurements of local attenuation, absorption, scattering and backscattering coefficient spectra in turbid media within the visible wavelength range (480 to 700 nm) [1–3]. LCS distinguishes itself from other quantitative spectroscopic techniques by controlling the photon path length of the detected light, which offers the unique possibility to control the measurement volume both in size and in depth—e.g. for the *in vivo* measurement of hemoglobin concentrations within distinct regions of the human dermal microcirculation [3]. Our previous studies on LCS involved a time-domain detection setup (tdLCS). However, from optical coherence tomography (OCT) studies, we know that spectral domain detection allows for more sensitive measurements, or higher acquisition speed at unaltered sensitivity [4,5]. Since clinical applications of LCS require both fast and sensitive measurements, we investigate the possibility for spectral domain detection in LCS (sdLCS), focusing primarily on validating a new method of analysis that was developed for this purpose.

Signal acquisition in sdLCS is comparable to that in spectrometer-based, spectral domain OCT (sdOCT), with the major difference that in sdLCS optical property spectra are derived from the spectral content of the signal, and in sdOCT an image is reconstructed from the backscattered intensity. To obtain optical property spectra within confined tissue volumes, sdLCS requires both high spatial and high spectral resolution. The spatial resolution for the acquisition of one backscattered spectrum in sdLCS and sdOCT is limited by the axial measurement range of the spectrograph, which depends on the spectral resolution of the spectrograph. Since the standard methods for signal acquisition in sdOCT commonly result in only one backscattered spectrum within the entire axial measurement range of the spectrograph (typically 1 to 2 mm) [4,5], the spatial resolution of these methods is not sufficient for sdLCS (typically 22 µm) [1–3]. Spectroscopic sdOCT methods solve this problem typically by windowed Fourier transforms on the measured spectrum, which result in multiple depth resolved spectra [6–8]. Due to the sensitivity decrease with depth inherent to these methods and the absence of focus tracking, these methods may not achieve optimal sensitivity in depth. In addition, precise refractive index-dependent corrections for the unwanted signal attenuation due to these effects are needed, in order to achieve quantitative measurements of the tissue attenuation. Therefore, we developed a method for sdLCS that applies focus tracking and measures with maximum spectrograph sensitivity (around zero delay) at every depth.

Our approach involves acquisition of local back scattered spectra within an axial measurement range of only 22 µm. Translation of this axial measurement range through the sample results in depth-resolved backscattered spectra acquired around zero delay with high spatial and sufficiently high spectral resolution (6 nm) while focus tracking is applied. The main challenge in our approach to sdLCS is to isolate the sample's backscattered spectrum from the detected spectrum, in order to retrieve the spectral absorption and backscattering features from the sample only. For this purpose, the unwanted DC and modulation components in the detected spectrum can be efficiently removed by introducing a phase modulation in the reference arm [9,10], for which we use an oscillating reference mirror.

Since the primary aim of this study is to validate whether we can use this new approach for the determination of local absorption and scattering coefficient spectra, we will provide proof of principle with an on-the-shelf spectrograph (USB4000, Ocean Optics, USA). Only part of the feasible speed advantage will be demonstrated, since the quantum efficiency and acquisition speed of this spectrograph are not optimized for sdLCS. We will validate our algorithm with a simulation of an sdLCS absorption measurement, while simulating the USB4000 as the detecting spectrograph. Subsequently, we experimentally demonstrate the

#171508 - $15.00 USD Received 27 Jun 2012; revised 6 Aug 2012; accepted 13 Aug 2012; published 27 Aug 2012

ability of sdLCS to measure the attenuation, absorption and scattering coefficient spectra from a polystyrene-dye phantom, and we compare our results to those of a tdLCS measurement.

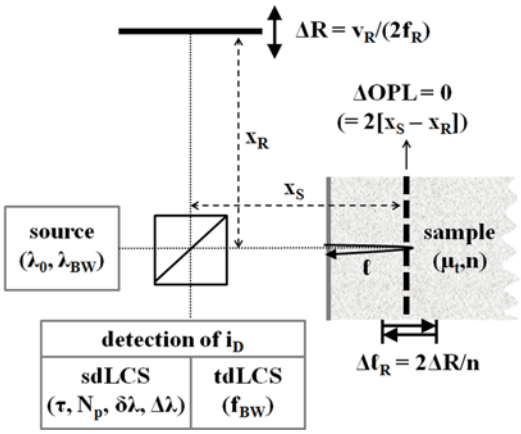

Fig. 1. Schematic illustration of setup and parameters in sdLCS/tdLCS. λ_0: center wavelength, λ_{BW}: spectral bandwidth, x_R: reference arm length, x_S: sample arm length, ΔOPL: path length difference, ΔR: reference mirror scanning range, v_R: reference mirror scanning velocity, f_R: reference mirror scanning frequency, ℓ: geometrical path length in sample, $\Delta\ell_R$: scanning window in sample induced by ΔR, n: refractive index, μ_t: attenuation coefficient, i_D: detector current, τ: integration time, N_p: number of pixels, δλ: pixel width, Δλ: wavelength resolution.

2. Theory

2.1. Background

For sdLCS, we use a setup that is based on a Michelson interferometer and a broad band light source (Fig. 1). A spectrograph detects the spectrum i_D, which (for a single reflector) is modulated by the optical path length difference between the sample arm and the reference arm $\Delta OPL = 2(x_S - x_R)$, with sample arm length x_S and reference arm length x_R:

$$i_D(k) \propto I_S(k) + I_R(k) + \sqrt{I_S(k) \cdot I_R(k)} \cdot 2\cos(k \cdot \Delta OPL), \qquad (1)$$

where k is the wavenumber ($k = 2\pi/\lambda$) and I_S and I_R are the signal intensities from the sample and reference arm, respectively.

Since we use sdLCS for doing spectroscopy, we are interested in the spectrum $I_S(k)$. The sample arm contribution $I_S(k)$ to $i_D(k)$ is related to the sample's backscattered power spectrum **S**, which can be obtained from $i_D(k)$ using the procedure described in Section 2.2. Note that all bold faced characters in this article represent wavelength (λ) dependent parameters. By adjusting x_R, we can control the geometrical round-trip path length ℓ in the sample at which we obtain **S** and by step-wise alteration of ℓ, we obtain a data set **S**(ℓ) [1–3]. Subsequently, we use a single exponential decay model to obtain the attenuation coefficient spectrum $\boldsymbol{\mu_t}$ of the sample:

$$\mathbf{S}(\ell) = \boldsymbol{\alpha}\, e^{-\boldsymbol{\mu_t} \cdot \ell}, \qquad (2)$$

assuming local sample homogeneity for all path lengths in the data set **S**(ℓ). The model is fitted to **S**(ℓ) with free running fit parameters ($\boldsymbol{\alpha}$ and $\boldsymbol{\mu_t}$), similar to our analysis for tdLCS [1–3]. The contributions of the scattering coefficient $\boldsymbol{\mu_s}$ and the absorption coefficient $\boldsymbol{\mu_a}$ can be obtained by fitting their individual contributions to the measured $\boldsymbol{\mu_t}$, as described in Ref. [3].

The axial measurement range of the spectrograph is limited by its maximal measurable path length difference and sensitivity roll-off in depth [4]. Therefore, the spectra **S**(ℓ) are acquired within a path length window Δℓ, which determines the spatial resolution for the $\boldsymbol{\mu_t}$-determination (see Section 2.3). Since a small axial measurement range is related to low

#171508 - $15.00 USD Received 27 Jun 2012; revised 6 Aug 2012; accepted 13 Aug 2012; published 27 Aug 2012

spectral resolution [11], a tradeoff exists between spectral and spatial resolution in sdLCS. However, we will show in this article that by selecting the right spectrograph, both sufficiently high spectral (6 nm) and spatial resolution (axial: 22 µm) can be achieved.

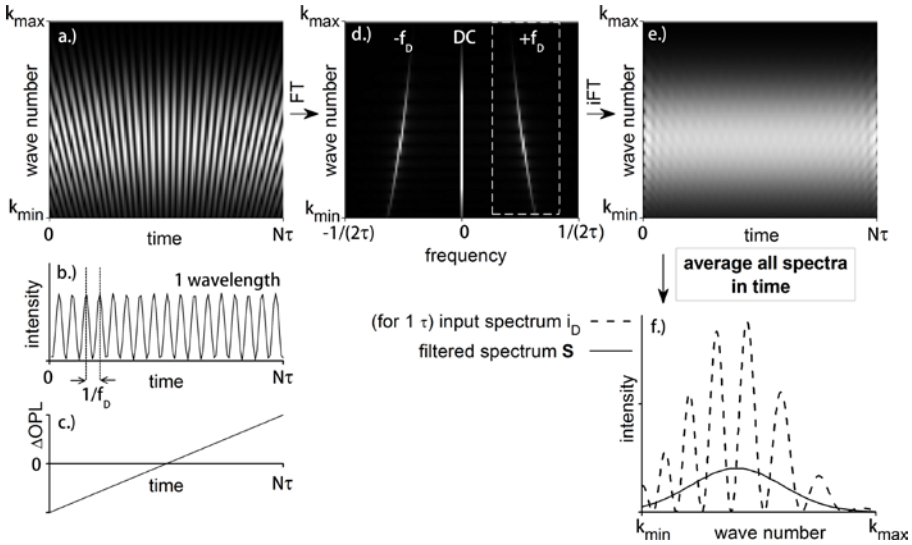

Fig. 2. Signal acquisition and processing in sdLCS. See Section 2.2 for details.

2.2. Removal of the DC and modulation terms

The sample's backscattered spectrum $\mathbf{S}(\ell)$ in Eq. (2) cannot be obtained directly from $i_D(k)$, because $i_D(k)$ contains unwanted DC (i.e. non-modulated components) and modulation components (Eq. (1). Since the spectral features in **S**—originating from the sample's characteristic absorption and backscattering—may exhibit oscillation frequencies similar to the modulation on $i_D(k)$, **S** cannot be directly obtained from $i_D(k)$. Similar to the method described for OCT in Ref. [9], we will isolate **S** from $i_D(k)$ by phase modulation and frequency domain filtering of the signal.

We start by modulating $i_D(k)$ using an oscillating mirror in the reference arm of our LCS system. This introduces a Doppler shift f_D for every wavelength: $f_D = 2v_R/\lambda = 2\Delta R \cdot f_R \cdot k/\pi$, with v_R the velocity, f_R the oscillation frequency and ΔR the scanning range in one direction of the reference mirror. Acquisition of N spectra $i_D(k)$ over a time interval $N(\tau + \tau_d)$ with integration time τ and dead time τ_d results in a data set $i_D(k,t)$, as illustrated in Fig. 2(a). Since τ_d (12 µs) $<<$ τ (6 ms) for the measurements described in this manuscript, we apply $N(\tau + \tau_d) \approx N\tau$ in the remaining part of our analysis. The frequency of the modulation on $i_D(k,t)$ changes as a function of time, because the movement of the reference mirror induces a change in ΔOPL (vertical direction in Fig. 2(a)). Figure 2(b) illustrates the time-modulation on $i_D(k,t)$ by f_D for one wavelength (horizontal direction in Fig. 2(a)). Since the sensitivity of the measurement is largest around ΔOPL = 0 or 'zero delay' (see Eq. (3), the range of ΔOPL is chosen such that it crosses zero delay at ½Nτ (Fig. 2(c)). Adequate sampling of the time-modulation on $i_D(k,t)$ is determined by the Nyquist criterion, i.e. the sampling frequency $f_s = 1/\tau$ needs to be larger than $2f_{D,max}$ (the largest value of f_D within the investigated spectral range). For the integration time, this results in $\tau < \pi/(2v_R k_{max}) = \lambda_{min}/(4v_R)$, with k_{max} the largest wave number and λ_{min} the shortest wavelength within the investigated spectral range.

Fourier transformation on $i_D(k,t)$ with respect to time provides the frequency content of the signal $i_D(k,f)$, which contains the modulation frequency f_D, its mirror image and a DC component (Fig. 2(d)). By filtering out the part of $i_D(k,f)$ containing only the positive frequencies + f_D, the unwanted DC component and the negative frequencies $-f_D$ are lost. Inverse Fourier transformation on the filtered $i_D(k,f)$ with respect to f provides a smooth, non-

#171508 - $15.00 USD Received 27 Jun 2012; revised 6 Aug 2012; accepted 13 Aug 2012; published 27 Aug 2012

modulated $i_D(k,t)$ that is confined in both amplitude and phase (Fig. 2(e)). Averaging of $i_D(k,t)$ over time results in the final spectrum **S** that we can use for the determination of $\boldsymbol{\mu}_t$ (Fig. 2(f)). A computational validation of this method will be shown by means of a simulation in Section 3.3.

2.3. The path length window Δℓ in sdLCS

In our approach for sdLCS, the path length window $\Delta\ell$ over which $\mathbf{S}(\lambda)$ is acquired results from a convolution of the reference mirror scanning window $\Delta\ell_R$ in the sample ($\Delta\ell_R = 2\Delta R/n$, with n the refractive index of the sample), with the path length window that is probed by the spectrograph $\Delta\ell_S$. In practice, this path length window can be approached with $\Delta\ell = \Delta\ell_R + \Delta\ell_S$ (inset of Fig. 3). The spectrograph probing window $\Delta\ell_S$ depends on the maximal measurable path length difference by the spectrograph ΔOPL_{max} (or imaging depth $d_{max} = \frac{1}{2}\Delta OPL_{max}$) and the sensitivity roll-off with ΔOPL of the spectrograph. Due to the Nyquist criterion, $\Delta OPL_{max} = 2\pi/\delta k$ with 'pixel resolution' $\delta k = (k_{max}-k_{min})/N_p$ and N_p the number of pixels of the spectrograph. The sensitivity roll-off of the spectrograph can be calculated using [11]

$$I(\Delta OPL) = \frac{\sin^2\left(\pi\Delta OPL/[2\Delta OPL_{max}]\right)}{\left(\pi\Delta OPL/[2\Delta OPL_{max}]\right)^2}\cdot\exp\left(-\frac{\pi^2\left(\Delta k/\delta k\right)^2}{8\ln 2}\left(\frac{\Delta OPL}{\Delta OPL_{max}}\right)^2\right), \quad (3)$$

in which Δk is the spectral resolution of the spectrograph, assuming a Gaussian beam profile.

For our sdLCS experiments, we use a spectrograph with a sensitivity roll-off that is two orders of magnitude smaller than ΔOPL_{max} (Section 3.1). Therefore, we can approach $\Delta\ell_S$ with the full width half max (FWHM) of the roll-off function: $\Delta\ell_S = FWHM_{roll\text{-}off}/n$. Hence, the path length window in sdLCS that determines the spatial resolution of the measurements is determined by: $\Delta\ell = \Delta\ell_R + \Delta\ell_S = (2\Delta R + FWHM_{roll\text{-}off})/n$.

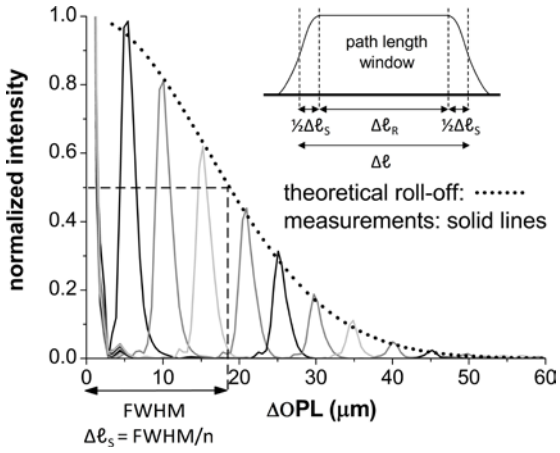

Fig. 3. Theoretical and measured sensitivity roll-off of the spectrograph. Inset: illustration of the path length window $\Delta\ell$ in sdLCS (Section 2.3).

2.4. Sensitivity/speed analysis

The SNR of any shot-noise limited LCS system is given by

$$\mathbf{SNR} = \frac{\boldsymbol{\varepsilon}\mathbf{S}}{h\nu f_{BW}} = \frac{\mathbf{S}}{h\nu}\times\begin{cases}\boldsymbol{\varepsilon}_{\mathbf{SD}}\boldsymbol{\tau} = \dfrac{\boldsymbol{\varepsilon}_{\mathbf{SD}}}{f_{scan,SD}} & \text{(sdLCS)}\\ \boldsymbol{\varepsilon}_{\mathbf{TD}}\dfrac{\lambda_0}{f_0\lambda_{BW}} = \boldsymbol{\varepsilon}_{\mathbf{TD}}\dfrac{\lambda_0^2}{2v_R\lambda_{BW}} = \dfrac{\boldsymbol{\varepsilon}_{\mathbf{TD}}}{f_{scan,TD}}\dfrac{\lambda_0^2}{2L_{scan,TD}\lambda_{BW}} & \text{(tdLCS)}\end{cases}. \quad (4)$$

#171508 - $15.00 USD Received 27 Jun 2012; revised 6 Aug 2012; accepted 13 Aug 2012; published 27 Aug 2012

Here, $\boldsymbol{\varepsilon}$ is the detector quantum efficiency; hv is the photon energy and f_{BW} is the electronic detection bandwidth of the system [5]. For a spectral domain (sdLCS) system, $f_{BW} = 1/\tau$ [4]. For a time domain (tdLCS) system, f_{BW} is determined by the imposed Doppler frequency $f = 2v_R/\lambda = 2L_{scan,TD} \cdot f_{scan,TD} /\lambda$ of the scanning reference mirror [1], with v_R its velocity, $L_{scan,TD} = 2\Delta R$ its scanning range in air and $f_{scan,TD} = f_R$ its scanning frequency. A commonly used comparison results in an improved SNR with a factor N_p (number of spectrograph pixels) for sdLCS compared to tdLCS [4,5,12], provided that $\boldsymbol{\varepsilon}$, L_{scan} and the f_{scan} (i.e. acquisition speed) are equal for both methods.

For a more generalized comparison between sdLCS and tdLCS, we take into account the differences in quantum efficiency, scan speed and scan range of the two methods (λ_0 and λ_{BW} are equal since we employ the same light source):

$$\mathbf{SNR_{SD}} = N_p \left(\frac{\boldsymbol{\varepsilon_{SD}}}{\boldsymbol{\varepsilon_{TD}}} \right) (2 f_R \tau) \left(\frac{2\Delta R}{\Delta L_{max}} \right) \mathbf{SNR_{TD}}, \qquad (5)$$

with ΔL_{max} the maximal measurable path length difference by the spectrograph after removal of the DC and modulation terms.

3. Materials and methods

In order to validate our data acquisition and analysis approach for sdLCS, we simulated an absorption measurement with the data acquisition parameters of our experimental setup. In addition, we measured attenuation spectra $\boldsymbol{\mu_t}$ from 480 to 700 nm on a phantom with known absorption $\boldsymbol{\mu_a}$ and scattering $\boldsymbol{\mu_s}$ coefficient spectra and we separated the individual contributions of $\boldsymbol{\mu_a}$ and $\boldsymbol{\mu_s}$ from the measured $\boldsymbol{\mu_t}$. To compare sdLCS to tdLCS, we performed a signal to noise analysis for both systems and repeated the phantom measurement with the tdLCS system described in detail in Ref. [1].

3.1. System and acquisition

The sdLCS system described in this article is identical to the tdLCS system with a low-pass filtered supercontinuum light source (SC430-4, Fianium Ltd., UK) described in Ref. [1–3], except for the detection end of the system, which consists of a spectrograph rather than a photodiode/lock-in amplifier combination. Hence, the multimode detection fiber is connected to the detecting spectrograph (USB4000, Ocean Optics, USA), with λ_{min} = 345 nm, λ_{max} = 1042 nm and N_p = 3648.

For both the sdLCS and tdLCS measurements, we controlled ℓ (ℓ = 0 – 2000 µm, with ℓ = 0 the sample surface) by translating the reference mirror in steps of 27 µm. By translating the sample in the axial direction, focus tracking of the spot size (r = 4.5 µm) in the sample was achieved. At every ℓ, back scattered power spectra $\mathbf{S}(\ell)$ were obtained over a path length window in the sample of $\Delta\ell$ = 43 µm for sdLCS (see Section 3.2) and $\Delta\ell$ = 44 µm for tdLCS [1]. For both sdLCS and tdLCS, $\mathbf{S}(\ell)$ was temporally averaged (N = 250 spectra per ℓ) and corrected for the background (i.e. the LCS spectrum obtained from the non-scattering glass of the inner cuvette wall of the sample). The integration time was set at the minimal stable integration time of this spectrograph, τ = 6 ms. To meet the sampling frequency requirement (Section 2.2), the velocity of the reference mirror was set at v_R = 12 µm/s (frequency f_R = 0.3 Hz, scanning range ΔR = 20 µm). The acquisition settings for the tdLCS measurements were identical to the settings in Ref. [1–3]. For both sdLCS and tdLCS, the most important acquisition parameters have been summarized in Table 1. Note that the acquisition speed for one temporally averaged spectrum $\mathbf{S}(\ell)$ is 3.6 times faster for sdLCS.

As described in Section 2, fitting the single exponential decay model $\mathbf{S}(\ell) = \boldsymbol{\alpha} \cdot \exp(-\boldsymbol{\mu_t} \cdot \ell)$ (free running fit parameters $\boldsymbol{\alpha}$ and $\boldsymbol{\mu_t}$) to the sdLCS and tdLCS acquired $\mathbf{S}(\ell)$ vs. ℓ, results in a $\boldsymbol{\mu_t}$ spectrum for both detection methods [1–3]. Uncertainties in $\boldsymbol{\alpha}$ and $\boldsymbol{\mu_t}$ are estimated by their 95% confidence intervals (c.i.). Since the spectral resolution in sdLCS ($\Delta\lambda$ = 6 nm) is higher than the pixel width of 0.2 nm, $\mathbf{S}(\ell)$ was binned into wavelength regions of 6 nm for the

#171508 - $15.00 USD Received 27 Jun 2012; revised 6 Aug 2012; accepted 13 Aug 2012; published 27 Aug 2012

sdLCS measurements. The values of $\boldsymbol{\mu_a}$ and $\boldsymbol{\mu_s}$ were obtained by fitting their individual contributions to the measured $\boldsymbol{\mu_t}$, as described in Ref. [3].

Table 1. Acquisition settings for sdLCS and tdLCS

Acquisition parameter	sdLCS	tdLCS
$\Delta\ell$	43 μm	44 μm
$\Delta\lambda$	6 nm (all λ)	4 nm @ λ = 480 nm 9 nm @ λ = 700 nm
v_R	0.006 mm/s	1.84 mm/s
f_R	0.3 Hz	23 Hz
ΔR	20 μm	40 μm
N = # averages per ℓ	250	250
Acquisition time of $\mathbf{S}(\ell)$	$N\tau$ = 1.5 s	$N/(2f_R)$ = 5.4 s

3.2. System characterization

Using the specifications of the spectrograph and the theory described in Section 2.3, we calculated that ΔOPL_{max} = 1880 μm. After measuring the spectral resolution of $\Delta\lambda$ = 6 nm with a 543 nm and 633 nm HeNe laser line, we used Eq. (3) to calculate that the $FWHM_{roll\text{-}off}$ is 18 μm ('theoretical' roll-off in Fig. 3). This $FWHM_{roll\text{-}off}$ corresponds well with the experimentally measured roll-off function, measured from the reflection of a glass slide in the sample arm as a function of ΔOPL between the sample arm and the reference arm (Fig. 3). Since the $FWHM_{roll\text{-}off}$ of the spectrograph is two orders of magnitude smaller than ΔOPL_{max}, the path length window that is probed by the spectrograph can be approximated with $\Delta\ell_S = FWHM_{roll\text{-}off}/n$ = 13 μm. Consequently, the total path length window that is probed in our sdLCS measurements is $\Delta\ell = \Delta\ell_R + \Delta\ell_S = (2\Delta R + FWHM_{roll\text{-}off})/n$ = 43 μm, with a fixed ΔR of 20 μm.

Based on Eq. (5), we can calculate the expected difference in SNR between both systems. The sdLCS spectrum covers approximately N_p = 1150 pixels on the USB4000. Based on a maximum number of 60 photons/count and a pixel well depth of 1.10^5 electrons given by the manufacturer, the quantum efficiency (QE = #electrons/photon) of the 16-bits USB4000 is 2.5% at 600 nm. Using the photodiode response of 0.43 A/W (2001, New Focus, USA), we can calculate that our tdLCS detector has a QE of 89% at 600 nm. With τ = 6 ms for our sdLCS system, the sensitivity advantage of the sdLCS measurements with the current equipment reduces to 0.38. Hence, when using the USB4000 as a detector for sdLCS with the settings in Table 1, we can expect a decrease in SNR of 4.2 dB at 600 nm with respect to tdLCS.

In order to compare the sensitivity of the current sdLCS system to the tdLCS system, we measured the SNR of the two detection methods, using a mirror behind an attenuating (2.0 optical density) filter in the sample arm. The optical power reference arm was optimized for (near) shot noise limited detection and the acquisition settings in Table 1 were applied. For both sdLCS and tdLCS, the spectrally resolved SNR was determined from the measured spectrum **S** at ΔOPL = 0 using [5]: SNR = 10·log(**S**/var[noise]). Here, var[noise] denotes the variance of the noise spectrum, measured with a ΔOPL large enough to observe no interference signal within the path length window $\Delta\ell$. For both detection methods, the measured SNR is around 75 dB per wavelength bin between 480 and 550 nm. After 550 nm, the SNR of tdLCS increases to a value of 85 dB at 700 nm, which can be explained by the larger quantum efficiency of the photodiode in tdLCS for longer wavelengths. The SNR of sdLCS remains spectrally flat over the full wavelength region of 480 to 700 nm, resulting in an SNR of ~3 dB lower compared to tdLCS at 600 nm, which is close to the predicted value of 4.2 dB.

3.3. Simulation

To validate the analysis algorithm described in Section 2.2, we simulated an absorption measurement on a sample containing oxyhemoglobin [13]. With this simulation, we tried to mimic the reality of the acquisition as closely as possible; therefore we incorporated summation over the integration time for every spectrum while simulating reference mirror

#171508 - $15.00 USD Received 27 Jun 2012; revised 6 Aug 2012; accepted 13 Aug 2012; published 27 Aug 2012

movement, a discrete wavelength axis and a limited spectral resolution. As a consequence, dynamic effects on such as fringe washout are taken into account. The contributions of scattering and noise were neglected in the simulation.

The detecting spectrograph was simulated with the properties of the spectrograph used for our measurements, as well as the values for the integration time and reference mirror velocity. The source spectrum $\mathbf{S_0}$ was simulated as a Gaussian with center wavelength $\lambda_0 = 550$ nm and bandwidth $\lambda_{FWHM} = 140$ nm. To account for the spectral resolution ($\Delta\lambda$) of the spectrograph, we convolved the spectrum with a Gaussian with a full-width at half maximum of 6 nm. The simulated sample arm power fraction was $\eta_S = 0.1$, resulting in a reference arm power fraction of $\eta_R = 0.9$. Within each integration time, 16 time-separated spectra at different reference mirror positions were added to simulate an acquired spectrum. A total number of N = 125 acquired spectra was simulated over a time interval of $N\tau = 0.75$ s. The initial ΔOPL was set at -4.5 µm to achieve zero delay at $\frac{1}{2}N\tau$.

Since scattering was neglected in the simulation, the attenuation coefficient $\boldsymbol{\mu_t}$ of the sample can be simplified to the absorption coefficient $\boldsymbol{\mu_a}$. The spectrum $\mathbf{S}(\ell)$ was calculated at $\ell_1 = 2$ mm and $\ell_2 = 4$ mm inside the sample, corresponding to depths $d_1 = 1$ mm and at $d_2 = 2$ mm, respectively. We obtained the absorption coefficient of the sample using Beer's law (Eq. (2): $\boldsymbol{\mu_a} = -[\frac{1}{2}(\ell_2 - \ell_1)]^{-1} \cdot \ln[\mathbf{S}(\ell_2)/\mathbf{S}(\ell_2)]$.

3.4. Phantom

We prepared a phantom, consisting of 0.096 vol% NIST-certified polystyrene spheres (⌀ 602 ± 6 nm, Thermo Scientific, USA) and 10% magenta dye (Ecoline #337, Royal Talens, The Netherlands). The $\boldsymbol{\mu_s}$ of the polystyrene spheres was calculated using Mie theory and integrated over the size distribution of the spheres (2*SD), as described in Ref. [2]. and the $\boldsymbol{\mu_a}$ of the dye was determined in a separate transmission measurement on the dye only, as described in Ref. [1]. The measured tdLCS spectra are broadened by Doppler frequency shifts induced by the Brownian motion of the polystyrene spheres. Therefore, both reference spectra for $\boldsymbol{\mu_s}$ and $\boldsymbol{\mu_a}$ were convolved with a Lorentzian with a line width of 9 nm for adequate comparison to the LCS spectra [1–3]. For the sdLCS measurements, Brownian motion does not influence the spectrum **S**, because the Doppler shifted frequencies remain within the bounds of the frequency domain filter (Fig. 2(d)). Since the reference spectrum of $\boldsymbol{\mu_a}$ was obtained with the same spectral resolution as the LCS spectra, we did not broaden this spectrum. The reference spectrum of $\boldsymbol{\mu_s}$ was convolved with a Lorentzian with a line width of 6 nm ($\Delta\lambda$ of the spectrograph).

4. Results

4.1. Simulation

Figure 4 shows the result of the simulation described in Section 3.3. The $i_D(\lambda)$ at ℓ_1 and ℓ_2 show little influence of the sample's absorption (Fig. 4(a)). However, after frequency domain filtering of $i_D(\lambda)$, the resulting spectra **S** at ℓ_1 and ℓ_2 clearly show the presence of the oxyhemoglobin absorption peaks (Fig. 4(b)). From Fig. 4(c), we can conclude that our method

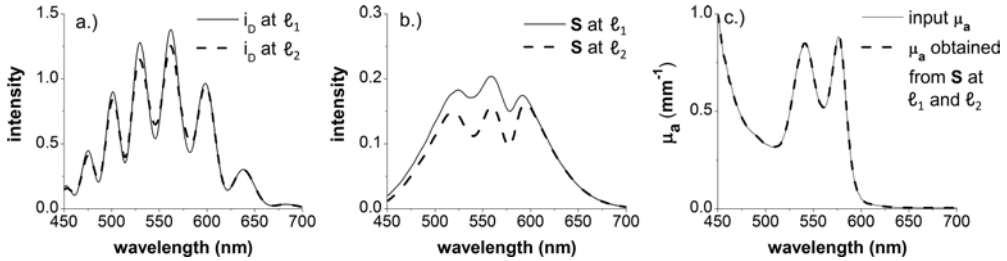

Fig. 4. Simulation of a $\boldsymbol{\mu_a}$ measurement in sdLCS. a.) input spectra i_D and b.) filtered spectra (**S**) at path lengths ℓ_1 and ℓ_2 inside the sample. c.) input $\boldsymbol{\mu_a}$ and recovered $\boldsymbol{\mu_a}$.

#171508 - $15.00 USD Received 27 Jun 2012; revised 6 Aug 2012; accepted 13 Aug 2012; published 27 Aug 2012

of data acquisition and analysis for sdLCS fully recovers the input $\boldsymbol{\mu_a}$ of this simulation. Even though the spectral features of the oxyhemoglobin absorption exhibit oscillations with a frequency comparable to that of the modulation on $i_D(\lambda)$, $\boldsymbol{\mu_a}$ is recovered without any artifacts.

4.2. Phantom

Figure 5 shows the measured $\boldsymbol{\mu_t}$ spectra by sdLCS and tdLCS on the polystyrene-dye phantom. The $\boldsymbol{\mu_t}$ spectra from both detection methods agree within the estimated uncertainties (error bars) for nearly all wavelengths. Also the fits on $\boldsymbol{\mu_t}$ and the $\boldsymbol{\mu_s}$-contributions to the fits agree well, and the $\boldsymbol{\mu_s}$-contributions are in good agreement with the Mie calculated $\boldsymbol{\mu_s}$. The fitted dye concentrations were 10.1 ± 0.4% for the sdLCS measurement and 9.5 ± 0.4% for the tdLCS measurement, which are both very close to the expected dye concentration of 10%. Note that part of the difference in spectral shape is caused by the presence of Brownian motion influences for tdLCS, versus the absence of it for sdLCS (Section 3.4).

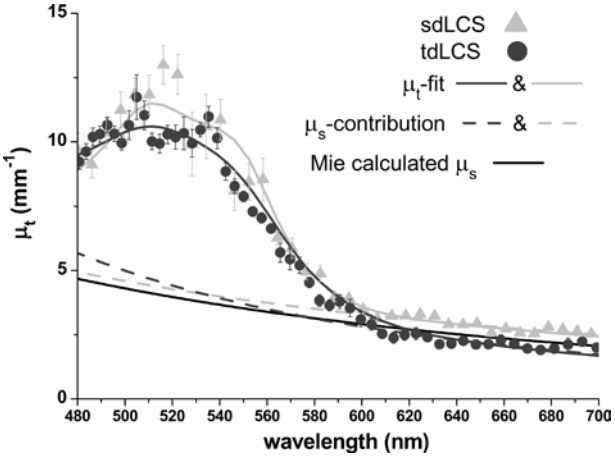

Fig. 5. Comparison of an sdLCS measurement to a tdLCS measurement of $\boldsymbol{\mu_t}$, $\boldsymbol{\mu_a}$ and $\boldsymbol{\mu_s}$ on a polystyrene-dye phantom.

5. Discussion and conclusion

In this article, we demonstrated and validated a new detection method and analysis algorithm for spectral domain detection in LCS. We showed that this method can be used for measuring local $\boldsymbol{\mu_t}$, $\boldsymbol{\mu_a}$ and $\boldsymbol{\mu_s}$ spectra in turbid media. The results of the sdLCS phantom measurement agreed well with the expected optical properties of the phantom and were comparable to the measured optical properties by tdLCS (Fig. 5). Whereas we did not explicitly show the localization aspect of our method by measuring on homogeneous media, previous studies with tdLCS proved that localized measurements of optical property spectra are possible within distinct tissue volumes [3].

The reason to validate this new detection method, is its theoretical sensitivity advantage compared to time domain detection (Section 2.4). As a consequence, the acquisition speed of the measurement can be reduced with respect to time domain detection, without reducing the signal to noise ratio. The sdLCS system that was validated in this article was more than three times faster than the tdLCS system, but not more sensitive (Section 3.2). A sensitivity advantage for sdLCS could not be demonstrated, because the quantum efficiency of the spectrograph is not optimized for these experiments. However, if the quantum efficiency would be similar to that of our tdLCS detector, the sensitivity advantage would be 11 dB at equal acquisition times for tdLCS and sdLCS (Eq. (5).

An additional shortcoming of the used spectrograph is its relatively slow acquisition speed (167 spectra/sec.). Slow acquisition speeds result in a decrease of the modulation depth in $i_D(\lambda)$ ('fringe wash-out'), due to the reference mirror movement induced change of ΔOPL

#171508 - $15.00 USD Received 27 Jun 2012; revised 6 Aug 2012; accepted 13 Aug 2012; published 27 Aug 2012

within the integration time. As a consequence, an additional decrease in sensitivity can occur, accounting for approximately 0.5 dB in our sdLCS system. Hence, not only higher quantum efficiency, but also faster acquisition speed is required to further improve the performance of our sdLCS system. Since high quantum efficiency line scan cameras are available with line rates up to 140 kHz, enhanced sensitivity and/or acquisition speed are realizable for sdLCS.

As we showed before for tdLCS, it may be advantageous to support the selection of the volume for optical property determination with an image of the investigated tissue volume [3]. Similar to tdLCS, this image can be reconstructed from the backscattered intensity as a function of depth. Our method for removal of the DC and modulation components in sdLCS also removes the 'mirror image' (complex ambiguity) when $\Delta OPL = 0$ is situated inside the sample. As a consequence, this method for sdLCS can be used to reconstruct an image without cross-talk between $i_D(\Delta OPL)$ and $i_D(-\Delta OPL)$ within the investigated path length window inside the sample.

The only technique that is reported to have comparable performance to our sdLCS system in terms of localized measurements of optical properties, is dual window sOCT that was developed by Robles et al. [8,14]. Whereas Robles et al. report that their method achieves higher resolution in both the spectral and the spatial domain by avoiding the inherent tradeoff between the two, their system may suffer from the effects of the sensitivity roll-off of the detecting spectrograph and the absence of focus tracking, which influence measurement depth. An advantage of our sdLCS system is that it does not rely on refractive index-dependent corrections for the unwanted signal attenuation due to these effects. This facilitates the exact determination of $\boldsymbol{\mu_s}$ and $\boldsymbol{\mu_a}$ contributions to the measured $\boldsymbol{\mu_t}$. Since the current spatial and spectral resolution of our sdLCS system are comparable to the tdLCS system (Table 1), the resolution of our system is sufficient to obtain relevant determinations of local tissue chromophore concentrations, e.g. within the dermis, or epidermis only as shown in Ref. [3].

In conclusion, we have demonstrated and validated a new approach for sdLCS, which has high potential to improve the accuracy and speed of localized optical property measurements by LCS. Undoubtedly, this will lead to improved clinical utility of the technique, e.g. for the non-invasive determination of blood composition (hemoglobin/bilirubin concentration and oxygen saturation).

Acknowledgments

This research is funded by personal grants in the Vernieuwingsimpuls program (D. J. F., AGT07544; M. C. G. A, AGT07547) by the Netherlands Organization of Scientific Research (NWO) and the Technology Foundation STW.